

High- and Low-Mass Star Forming Regions from Hierarchical Gravitational Fragmentation

Enrique Vázquez-Semadeni¹, Gilberto C. Gómez¹, A. Katharina Jappsen², Javier Ballesteros-Paredes¹ and Ralf S. Klessen³

Received _____; accepted _____

Submitted to ApJ

¹Centro de Radioastronomía y Astrofísica, Universidad Nacional Autónoma de México, Apdo. Postal 3-72, Morelia, Michoacán, 58089, México

²School of Physics & Astronomy, Cardiff University, Queens Buildings, The Parade, Cardiff CF24 3AA, UK

³Zentrum für Astronomie der Universität Heidelberg, Institut für Theoretische Astrophysik, 69120 Heidelberg, Germany

ABSTRACT

We investigate the properties of “star forming regions” in a previously published numerical simulation of molecular cloud formation out of compressive motions in the warm neutral atomic interstellar medium, neglecting magnetic fields and stellar feedback. In this simulation, a large cold atomic cloud forms by nonlinearly triggered thermal instability, and then becomes gravitationally unstable and begins contracting as a whole, but it undergoes hierarchical fragmentation in which local, isolated collapse events occur in a peripheral ring before the global collapse is completed, at which time a massive “cloud” is formed at the collapse center. We study the properties (density, total gas+stars mass, stellar mass, velocity dispersion, and star formation rate) of the cloud hosting the first local, isolated “star formation” event and compare them with those of the cloud formed by the central, global collapse event. In these simulations, the velocity dispersions at all scales are caused primarily by infall motions rather than by random turbulence. We suggest that the small-scale isolated collapses may be representative of low- to intermediate-mass star-forming regions, with gas masses (M_{gas}) of hundreds of solar masses, velocity dispersions $\sigma_v \sim 0.7 \text{ km s}^{-1}$, and star formation rates (SFRs) $\sim 10^{-4} M_{\odot} \text{ yr}^{-1}$, while the large-scale, massive ones may be representative of massive star forming regions, with M_{gas} of thousands of solar masses, $\sigma_v \sim$ a few km s^{-1} , and SFRs $\sim 10^{-3} M_{\odot} \text{ yr}^{-1}$.

We also obtain the statistical distributions of the physical properties of the dense cores appearing in the central region of massive collapse, and compare them with those from a recent survey of the massive star forming region in the Cygnus X molecular cloud by Motte et al. We find that the observed and simulated distributions are in general very similar, reinforcing the suggestion that massive star forming regions are sites of global, large-scale collapse. This

suggestion contrasts with the common notion that these regions are in rough virial equilibrium, supported by strong turbulence.

Subject headings: ISM: clouds — ISM: evolution — Stars: formation

1. Introduction

The formation of massive stars is currently a matter of intense debate (e.g., Zinnecker & Yorke 2007). High-mass star forming regions are characterized by more extreme physical conditions than their low-mass counterparts, containing cores of size, mass, and velocity dispersion roughly an order of magnitude larger than those of cores in low-mass regions (e.g. Jijina, Myers & Adams 1999; Lee & Myers 1999; Garay & Lizano 1999; Kurtz et al. 2000; Beuther et al. 2007). In particular, typical values of the properties of clumps within high-mass star forming regions (HMRs) are sizes 0.2–0.5 pc, mean densities $n \sim 10^5 \text{ cm}^{-3}$, masses between 100 and 1000 M_{\odot} , and velocity dispersions ranging between 1.5 and 4 km s^{-1} . In turn, the clumps break down into even denser “cores” that are believed to be the immediate precursors of single or gravitationally bound multiple massive protostars.

The high velocity dispersions of clumps in HMRs are generally interpreted as strong turbulence that manages to support the clumps against gravity (e.g., Garay & Lizano 1999; McKee & Tan 2003). However, the notion of “turbulent support” is difficult to maintain at the scales of these cores. Turbulence is a flow regime in which the largest velocity differences are associated with the largest separations (e.g. Frisch 1995), so that the largest turbulent velocity differences within a clump are expected to occur at scales comparable to that of the clump itself, thus being strongly anisotropic with respect to it, and definitely not “small scale”. This property is indeed observed in molecular clouds (Ossenkopf & Mac Low 2002; Brunt 2003).

Moreover, in the case of supersonic turbulence, the clumps are expected to be formed by large-scale compressive motions, so that the turbulence is likely to have a strong compressive component (Hunter & Fleck 1982; Ballesteros-Paredes et al. 1999a, 2003; Klessen et al. 2005; Federrath et al. 2008; Vázquez-Semadeni et al. 2008). In particular,

the latter authors presented a numerical study of clouds with random turbulence driving showing that, even with continuous random driving at large scales, there is a trend for the clumps to contain a net convergence of the flow, which contradicts the hypothesis that the non-thermal motions consist of isotropic, small-scale turbulence. After all, the clumps *must* be formed by a globally converging flow, as dictated by the continuity equation.

In addition, numerical simulations of cloud formation in the diffuse atomic ISM (e.g. Vázquez-Semadeni et al. 1995, 1996; Passot et al. 1995; Ballesteros-Paredes et al. 1999a,b; Koyama & Inutsuka 2002; Audit & Hennebelle 2005; Heitsch et al. 2005, 2006, 2008; Vázquez-Semadeni et al. 2006, 2007; Hennebelle & Audit 2007) and of star formation in turbulent, self-gravitating clouds (e.g. Klessen, Heitsch & Mac Low 2000; Heitsch, Mac Low & Klessen 2001; Klessen 2001; Bate, Bonnell, & Bromm 2003; Vázquez-Semadeni et al. 2005, 2007) show that the velocity fields are in general organized at all scales, exhibiting a continuity from the large scales outside the clumps all the way to their interiors. Specifically, the simulations of molecular cloud formation by Vázquez-Semadeni et al. (2007), hereafter Paper I, showed that, as the cloud’s mass is consumed by the formation of collapsed objects (“stars”), it continues to accrete mass from its surrounding, more diffuse (“atomic”) medium, the whole process amounting to a “mass cascade”, analogous to a turbulent energy cascade, as proposed by Newman & Wasserman (1990) and Field, Blackman, & Keto (2008). The latter authors, however, assumed that the cascade is punctuated by virialization at each scale, while numerical simulations such as those of Bate, Bonnell, & Bromm (2003), Paper I, and Heitsch et al. (2008) exhibit no such intermediate virialization stage, but just a hierarchical fragmentation process, as originally proposed by Hoyle (1953).

In this paper, we investigate the consequences of this hierarchical fragmentation scenario on the formation of low- and high-mass star forming regions, taking advantage

of the variety of star forming regions appearing in the main simulation of Paper I. In that paper, we speculated that the global contraction might be halted by stellar energy feedback before the global collapse was completed. However, in the present paper we reject that speculation, and take the simulation at face value, presenting a study of the physical conditions in the region where the global collapse finally converges, showing that they resemble the physical conditions of high-mass star forming regions, thus suggesting that such regions may be in generalized gravitational collapse rather than in a state of turbulent “support”, as proposed, for example, by Hartmann & Burkert (2007) for the Orion molecular cloud. Of course, the effect of stellar feedback cannot be neglected, but in the present paper we simply assume that the star formation occurring in the early stages of the simulation does not prevent the occurrence of a massive collapse at later times.

In §2 we briefly recall the main production and evolutionary features of the numerical simulation, and identify the regions we investigate. In §3 we measure the evolution of the total (dense gas + “stars”) and “stellar” masses, and the instantaneous star formation rate (SFR) in both the isolated, peripheral, low-mass region (LMR) and in the central, global-collapse HMR. In §4 we then compare our results with available observations. In §4.1 we compare the physical conditions and the star formation rates, showing that these indicators are reasonably similar to those of actual star forming regions of each type. Next, in §4.2 we perform a survey of the cores in our HMR, and compare the distributions of their sizes, masses and densities with those of a recent survey of the Cygnus X region by Motte et al. (2007), showing that the distributions are very similar. Finally, in §5 we discuss the limitations of our study and present a summary.

2. The numerical model

In this paper, we analyze data from the simulation labeled L256 Δv 0.17 in Paper I. We refer the reader to that paper for details. Here we just mention that it is an SPH simulation, performed with the GADGET code (Springel et al. 2001), including self-gravity and parameterized heating and cooling that imply a thermally bistable medium. The simulation uses 3.24×10^6 SPH particles, and uses the prescription by Jappsen et al. (2005) for forming “sink particles” at densities above a certain density threshold, which we take as $n_{\text{thr}} = 3.2 \times 10^6 \text{ cm}^{-3}$. Once formed, the sinks can continue to accrete mass from their surroundings. Note, however, that the sinks are not sufficiently resolved in mass to be considered individual stars, and should be considered stellar clusters instead.

The total mass in the simulation is $5.26 \times 10^5 M_{\odot}$, and the initial conditions correspond to a collision of streams of diffuse gas (of the same density as their surroundings) along the x -direction, which nonlinearly triggers thermal instability (Hennebelle & Pérault 1999), causing the formation of a dense, cold, flattened turbulent atomic cloud (Walder & Folini 2000; Koyama & Inutsuka 2002; Heitsch et al. 2005; Audit & Hennebelle 2005; Heitsch et al. 2006; Vázquez-Semadeni et al. 2006, 2007; Hennebelle & Audit 2007), which extends in the (y, z) plane of the simulation. The size of the numerical box is 256 pc, and the inflow velocity of the colliding streams is 1.22 times the adiabatic sound speed in the ambient gas, which has $T = 5000 \text{ K}$ and a mean density of $n = 1 \text{ cm}^{-3}$. The turbulent atomic cloud becomes gravitationally unstable and begins to contract gravitationally, eventually reaching densities typical of molecular gas, at which point we assume that the gas has become molecular. The cloud has a flattened shape during most of its evolution, and star formation begins at $t \sim 17 \text{ Myr}$ in the periphery of the cloud, since the global collapse of a finite sheet-like cloud proceeds from the outside in, as shown by Burkert & Hartmann (2004). By $t = 23.4 \text{ Myr}$, the global collapse is completed, although the residual turbulence

in the cloud causes the infall motions to have a random component, so that the collapse center spans several parsecs across. Animations showing the large-scale evolution of this simulation can be found in the electronic edition of Paper I.

In particular, we focus on two different regions of “star” (i.e., sink particle) formation. As a representative example of an LMR, we consider the first region to ever form stars in the peripheral ring starting at $t = 17.3$ Myr, which involves relatively small mass in both gas and sinks. As an example of an HMR, we consider the central region at which the global collapse converges at $t = 23.4$ Myr, which involves a substantially larger amount of mass, with the aim of determining whether they can be representative of low-mass and high-mass star forming regions, respectively.

Figure 1 shows a column density map of the LMR at $t = 19.1$ Myr. The image is integrated over 16 pc in the x -direction. In the electronic version of the paper, this image shows the evolution of this region from $t = 16.6$ to 19.9 Myr. The dots show the newly formed sink particles. Figure 2 shows images of the central 8 parsecs of the simulation (the HMR), at $t = 24.2$ Myr, viewed edge-on (*left*) and face-on (*right*). In the electronic version, this figure shows animations of the same region from $t = 22.6$ to 25.2 Myr for both views. In the images and animations of Fig. 2 we do not show the sink particles because a large number of previously formed particles is already present in the region, and it is not easy to see the particles formed there.

3. Physical conditions of the “low”- and “high”-mass regions

We begin our comparison study between the two regions by measuring the evolution of physical and star-forming properties of the “clouds” in these regions. To this end, we interpolate the SPH data of the regions shown in Figs. 1 and 2 onto a 256^3 grid in order to

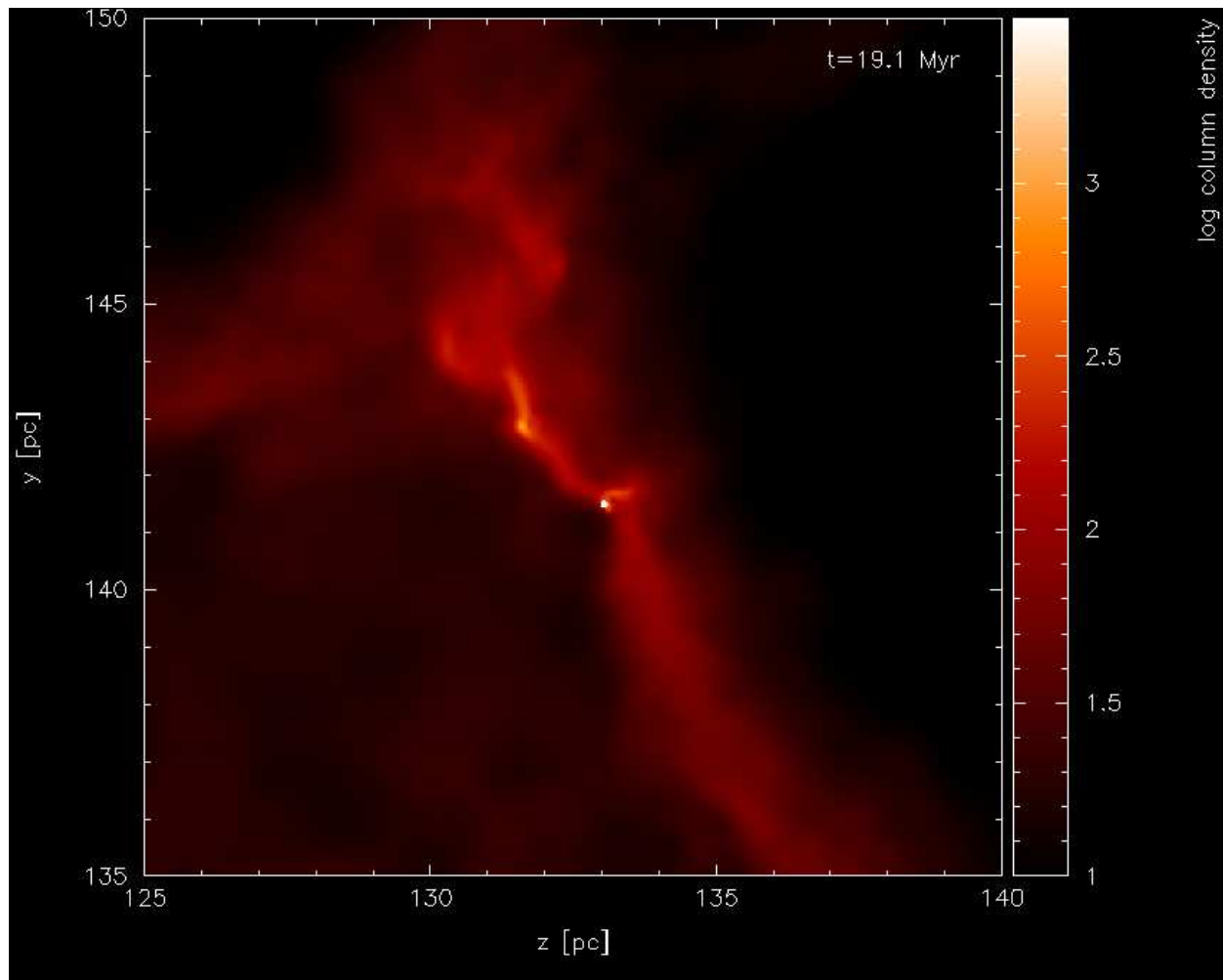


Fig. 1.— Column density plot of Cloud 1 in the y - z plane at $t = 19.1$ Myr, integrating over the central 16 pc along the x direction. The dots show the stellar objects (sink particles). The electronic version of this figure shows an animation of this region from $t = 16.6$ to 19.9 Myr. The column density is in code units, which correspond to $9.85 \times 10^{19} \text{ cm}^{-2}$. The dots represent sink particles.

manipulate the data with the IDL software. We then define the clouds as connected sets of pixels with densities above $n_{\text{th}} = 500 \text{ cm}^{-3}$. We refer to the resulting clouds as “Cloud 1” (C1) in the LMR, and “the Central Cloud” (CC) in the HMR. In Fig. 3 we compare the evolution of the physical properties of the two clouds over a few Myr. Note that the starting times (t_0) for the evolutionary plots are different in the two cases, being $t_0 = 17.27$ Myr for C1 and $t_0 = 22.58$ Myr for the CC. The *thick lines* correspond to the CC, and the *thin lines* correspond to C1. The *left column* shows the evolution of the density, size and velocity dispersion for the two clouds, where the size is calculated as $r = (3V/4\pi)^{1/3}$, V being the volume of the cloud.

From these figures we see that the CC clearly has larger density, size, velocity dispersion, and mass than C1, at least during the time spans shown the figures (C1 later acquires more mass and becomes more similar to the CC). Although the density of the CC is only a factor of 2 larger than that of C1 on average, we see that its size ranges between half and one order of magnitude larger than that of C1, and similarly for its velocity dispersion, which is on the order of a few km s^{-1} , as is the case for HMRs (e.g., Beuther et al. 2007). Similarly, the CC’s mass ranges in the thousands of solar masses, while that of C1 initially ranges in the hundreds, although, as mentioned above, this region is growing in time, and approaching the conditions of the CC at late times. Note that the gas mass in the CC is initially less than the sink mass because we include the mass of pre-existing sinks in the region, and not only the sinks formed by the CC. We do this because we next compute with the virial mass of the system, which must be compared with the total gravitational mass, including the gas and all sinks in the region.

We compute the virial mass of each region applying the standard formula

$$M_{\text{vir}} \equiv 210 \left(\frac{R}{\text{pc}} \right) \left(\frac{\Delta v_{\text{eff}}}{\text{km s}^{-1}} \right)^2 M_{\odot}. \quad (1)$$

It is noteworthy that the CC, even though it is in an extremely dynamic infalling state, has

a ratio of mass to virial mass M/M_J of almost exactly unity during most of its evolution. This is precisely what is expected for an object undergoing gravitational contraction, and has been observed previously in numerical simulations (e.g., Klessen & Burkert 2000, 2001; Vázquez-Semadeni et al. 2007). Instead, this ratio is completely arbitrary in the case of clouds or clumps formed purely by turbulent compressions.

Cloud 1, on the other hand, starts with a ratio of nearly 5, but it steadily approaches unity as it accelerates in its infall. Note that such values of this ratio are not uncommon in observed low-mass clouds (see, e.g., Tachihara et al. 2002; Morata et al. 2005). Presumably, the relatively large initial values of the ratio constitute an indication that at its initial states, the cloud is only beginning to decouple from the global flow, and starting its own collapse.

We furthermore measure the “star” formation rate (SFR) in both clumps, defined as

$$\text{SFR} = \frac{\Delta M_{\text{sink}}}{\Delta t}, \quad (2)$$

where ΔM_{sink} is the increment in sink mass in the region during the time interval $\Delta t = 0.13$ Myr between successive data dumps. Analogously, we define the “specific SFR” (sfr) as

$$\text{sfr} = \frac{\text{SFR}}{M_{\text{gas}}}, \quad (3)$$

where M_{gas} is the instantaneous dense gas mass in the region, again defined as the mass of gas with densities $n > 500 \text{ cm}^{-3}$. Note that, for simplicity, we perform these measurements directly on the SPH data, rather than on their interpolation on a grid. Note also that we use the increment in the mass of the sinks rather than in the number of sinks because, as mentioned in §2, our sinks are not sufficiently resolved in mass, and furthermore they continue to accrete mass after they form, as shown in Fig. 4. This figure shows the mass evolution of the most massive sinks formed in the simulation up to $t = 20$ Myr (*left panel*), the most massive sinks formed in the central 8-pc region for $23.9 < t < 25$ Myr (*middle panel*), and those formed outside of the central 8-pc region during the same time interval (*right panel*).

Both the SFR and the *sfr* are shown in Fig. 5. It is clearly seen that again, the SFR of the CC is roughly one order of magnitude larger than that of C1. However, it is seen that the *specific* star formation rate is similar for both clouds, suggesting that the larger SFR of the CC is due exclusively to the larger amount of mass available for collapse in this cloud. In any case, if one assumes a universal IMF, then the larger SFR of the CC implies that it has a ten-fold larger likelihood of forming massive stars, in correspondence with its more massive and violent status.

4. Comparison with observations

In this section we compare the massive star-forming region described in §3 to some well-known, massive star-forming regions in the Galaxy. We first focus on the mean physical properties and star formation rate of the CC with those of whole star-forming regions, and then we compare the physical properties of clumps and cores within it with those of the clumps and cores in the Cygnus X molecular cloud, as reported by Motte et al. (2007).

4.1. Physical properties and star formation rates

From Fig. 3, we see that, on average, the CC is characterized by a gas mass of $M_{\text{gas}} \sim 3000M_{\odot}$, a size of $r \sim 2.3$ pc, and a three-dimensional velocity dispersion $\sigma \sim 4$ km s⁻¹, implying a one-dimensional velocity dispersion of ~ 2.3 km s⁻¹. These values can be compared to the corresponding ones for OMC-1, the gas behind the Orion Nebula cluster in the Orion Molecular Cloud. According to Bally et al. (1987), the total gas mass in OMC-1 is $\sim 2200M_{\odot}$ and the typical observed (i.e., 1D) rms velocity is ~ 2 km s⁻¹, within a region of size ~ 2 pc. Thus, we see that the gas mass, size, and velocity dispersion of the CC match those of OMC-1 to within less than 50%, 20%, and 20%, respectively.

Moreover, from Fig. 5 we see that the CC is characterized by sink formation rate $\sim 10^{-3}M_{\odot} \text{ yr}^{-1}$ on average. Tobin et al. (2009) report on 1613 stars in the Orion Nebula Cluster. Taking this number as a proxy for the total stellar content of this region, and a mean mass of $0.3M_{\odot}$ (Hillenbrand & Carpenter 2000), this implies a total stellar mass of $\sim 500M_{\odot}$. The estimated age of the cluster is $\sim 1 \text{ Myr}$. We thus infer an SFR of $\sim 5 \times 10^{-4}M_{\odot} \text{ yr}^{-1}$, in reasonable agreement with our CC.

A similar analysis can be performed for the dense cores in OMC-1. Ikeda et al. (2007) report a total mass of dense cores in this region of $\sim 800M_{\odot}$. Assuming that these have typical lifetimes between 2 and $5 \times 10^5 \text{ yr}$ (e.g., Hatchell et al. 2007), implying a core formation rate between 1.6 and $4 \times 10^{-3}M_{\odot} \text{ yr}^{-1}$, which again compares very well to the mean value of the SFR shown in Fig. 5. Note that we find that the core formation rate in OMC-1 is larger than the SFR by a factor of a few, a reasonable result if the efficiency of star formation within the cores is smaller than unity. Moreover these values bracket our sink formation rate, which is also expected to be an upper limit to the actual star formation rate in the simulations, since our sinks are formed at core densities $n \sim 3 \times 10^6 \text{ cm}^{-3}$, at which the gas-to-stars efficiency is still expected to be smaller than unity.

4.2. Statistics of cores in the Central Cloud

As a further test of the similarity of the CC with high-mass star forming regions, in this section we compare the statistics of the dense cores within the CC with those reported by Motte et al. (2007) for the Cygnus X molecular complex. These authors have performed a 1.2 mm continuum survey of this region, and compiled a large dataset of 129 massive dense cores, of sizes $\sim 0.1 \text{ pc}$, masses $M_{1.2\text{mm}} = 4\text{--}950 M_{\odot}$, and densities $n \sim 10^5 \text{ cm}^{-3}$, listed in Table 1 of that paper.

In order to compare with these data, we identify dense cores within the gridded version of the central 8-parsec region of our simulation (cf. Fig. 2) at time $t = 23.9$ Myr. We apply a simple clump-finding algorithm based on identifying connected sets of grid points whose densities are above a certain threshold. In order to construct a suitable ensemble of cores, we consider a set of four thresholds, at $n = 10^4$, 3×10^4 , 10^5 , and 3×10^5 cm^{-3} . We do this in order to allow for a wider dynamic range in the physical properties of the cores, since our previous experience shows that objects selected with a given threshold have mean densities that differ by less than an order of magnitude from the value of the threshold (e.g., Vázquez-Semadeni, Ballesteros-Paredes & Rodríguez 1997). We choose this procedure for simplicity, and because larger clumps defined at lower thresholds may be bound structures themselves that should be taken into account. Motte et al. (2007) themselves used a combination of source extraction analysis and Gaussclumps (Stutzki & Güsten 1990).

This procedure leaves us with 39 cores, 38 of which have $M > 4M_{\odot}$. For each core, we measure its mass, mean density, and velocity dispersion, and estimate its size as $r \approx (3V/4\pi)^{1/3}$, where V is its volume. The distributions of these properties can be compared with those reported by Motte et al. (2007). We show the distribution of their properties in the histograms presented in Fig. 6 by the *dotted* lines. Superimposed on these histograms, the *solid* lines show the corresponding distributions for the 38 cores more massive than $4M_{\odot}$ in the central 8 parsecs of our simulation. We see that the distributions match extremely well for size, mass, and mean density. No comparison is made for the velocity dispersions because Motte et al. (2007) do not report them, but in our sample, they range from ~ 0.2 to ~ 3 km s^{-1} .

A final comparison that can be made is at the “clump” level. Motte et al. (2007) report their typical sizes, masses, and densities to be $r \sim 0.8$ pc, $M \sim 1000M_{\odot}$, and $n \sim 7 \times 10^3$ cm^{-3} respectively (see their abstract and column 3 in their Table 4). If we

threshold our central-8-pc data at a density $7 \times 10^3 \text{ cm}^{-3}$, we obtain a structure, shown in Fig. 7, of size $r \approx 1.0 \text{ pc}$ and a mass of $2911M_{\odot}$, in good agreement with the typical values reported by those authors.

5. Conclusions

In this paper we have presented numerical evidence that the physical conditions in low- and high-mass star forming regions (“clouds”) can arise from hierarchical gravitational collapse, with the former regions arising from small-scale fragments in the collapse (which however occur first, because they originate from local high-amplitude density fluctuations which have a shorter free-fall time), while the latter may appear when the global, large-scale collapse is completed. The local collapse events do not exhaust the gas in their regions because a) the consumption time is relatively long, $\sim 5 \text{ Myr}$ (cf. Fig. 5, *right panel*), and b) because the clouds continue to accrete mass from their atomic surroundings throughout their evolution. Thus, the isolated low-mass clouds eventually collide to form a high-mass complex. In this scenario, velocity dispersions are caused primarily by infall motions rather than random turbulence, but its hierarchical nature may explain why massive cores tend to have larger velocity dispersions than low-mass ones at the same size (see, e.g., Fig. 10 of Garay & Lizano 1999), since the former only begin contracting when they decouple from the global flow, while the latter have been accelerating in their contraction for a longer time.

The evidence we presented consists of two parts. First, we analyzed the evolution of the physical properties (mass, mean density, size, velocity dispersion, and mass to virial mass ratio), as well as of the SFRs of two examples of the class of objects, which we called “Cloud 1” (C1) and “the Central Cloud” (CC). We noted that the latter, which forms as a consequence of the large-scale collapse of the cloud complex in the simulation, has properties consistent with those of high-mass regions (HMRs), such as a gas mass $M_{\text{gas}} \sim 3000M_{\odot}$,

a velocity dispersion σ_v of a few km s^{-1} , and a star formation rate $\text{SFR} \sim 10^{-3} M_\odot \text{yr}^{-1}$, while C1 is more reminiscent of low- or intermediate-mass regions, with $M_{\text{gas}} \sim 400 M_\odot$, $\sigma_v \sim 0.7 \text{ km s}^{-1}$ (during its initial stages, as it later becomes more massive), and $\text{SFR} \sim 10^{-4} M_\odot \text{yr}^{-1}$.

Secondly, we performed a survey of the dense cores in the massive cloud (the central 8 parsecs of the simulation at the time the large-scale collapse converges there), and compared their statistical properties with those reported for the dense cores in the Cygnus X cloud complex by Motte et al. (2007), finding that the distributions of both samples match each other very well. At the slightly larger-scale, “clump” level, we also found good agreement between the mean properties reported by those authors and the “clump” in that region. These results suggest that indeed the convergence of the global collapse is a good model of HMRs.

Our simulation clearly has the caveat that it did not include magnetic fields nor energy feedback from the newly formed stars, and thus it cannot be considered conclusive evidence that star formation in giant cloud complexes occurs via this proposed hierarchical fragmentation mechanism. However, our results are consistent with recent suggestions, based on comparisons between simulations and observations, that molecular clouds (e.g., Hartmann & Burkert 2007) and clumps (e.g. Peretto, Hennebelle & André 2007) may be in a state of gravitational collapse. If confirmed, these suggestions point towards a return to the original suggestion by Goldreich & Kwan (1974) that the observed linewidths in molecular clouds are due primarily to gravitational contraction. This suggestion was dismissed by Zuckerman & Palmer (1974) through the argument that this would imply a much larger average star formation rate in the Galaxy than observed. However, it is possible that this criticism may be overcome if magnetic field fluctuations in the clouds imply that some parts of them are magnetically supported so that only the non-supported parts parts

of the clouds undergo collapse (Hartmann, Ballesteros-Paredes, & Bergin 2001; Elmegreen 2007), and the star formation rate is then regulated by stellar feedback, with globally collapsing motions arising only for those regions that manage to “percolate” through the field fluctuations and the stellar-feedback motions.

The numerical simulation was performed in the cluster at CRyA-UNAM acquired with CONACYT grants to E.V.-S. 36571-E and 47366-F. The animations were produced using the SPLASH visualization tool (Price 2007). We thankfully acknowledge financial support from CONACYT grants 47366-F to E. V.-S. and 50402-F to G. C. G., UNAM-PAPIIT grant 110606 to J. B.-P. R.S.K. thanks the German Science Foundation (DFG) for support via the Emmy Noether grant KL 1358/1, as well as via grants KL 1358/4 and KL 1358/5, and via SFB 439 “Galaxies in the Early Universe”. R.S.K. also acknowledges subsidies from the FRONTIER program of Heidelberg University.

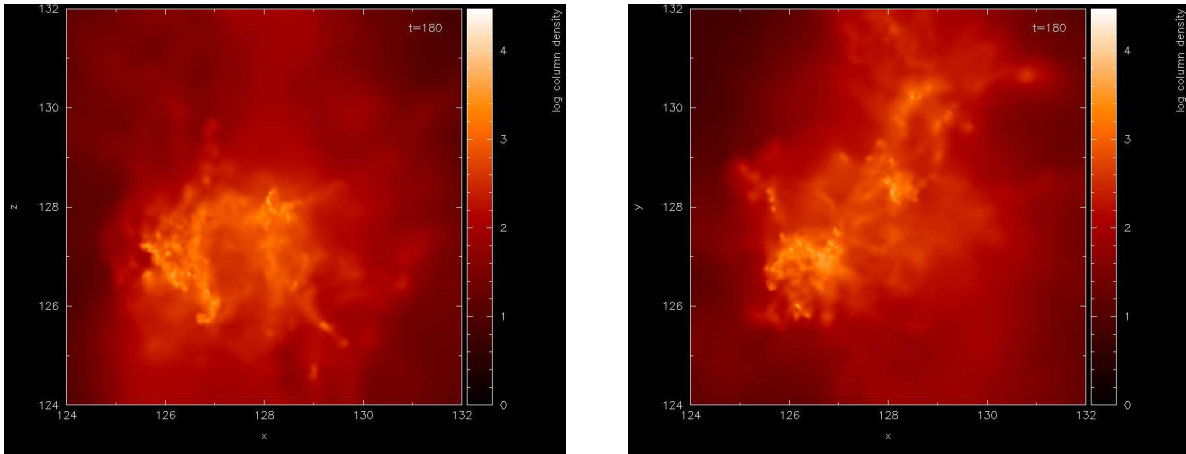


Fig. 2.— Two views of the central 8-pc cubic region. *Left panel:* Column density integrated along the z direction. *Right panel:* Column density integrated along the y direction. The electronic version of this image shows the evolution of these regions from $t = 22.6$ to 25.2 Myr.

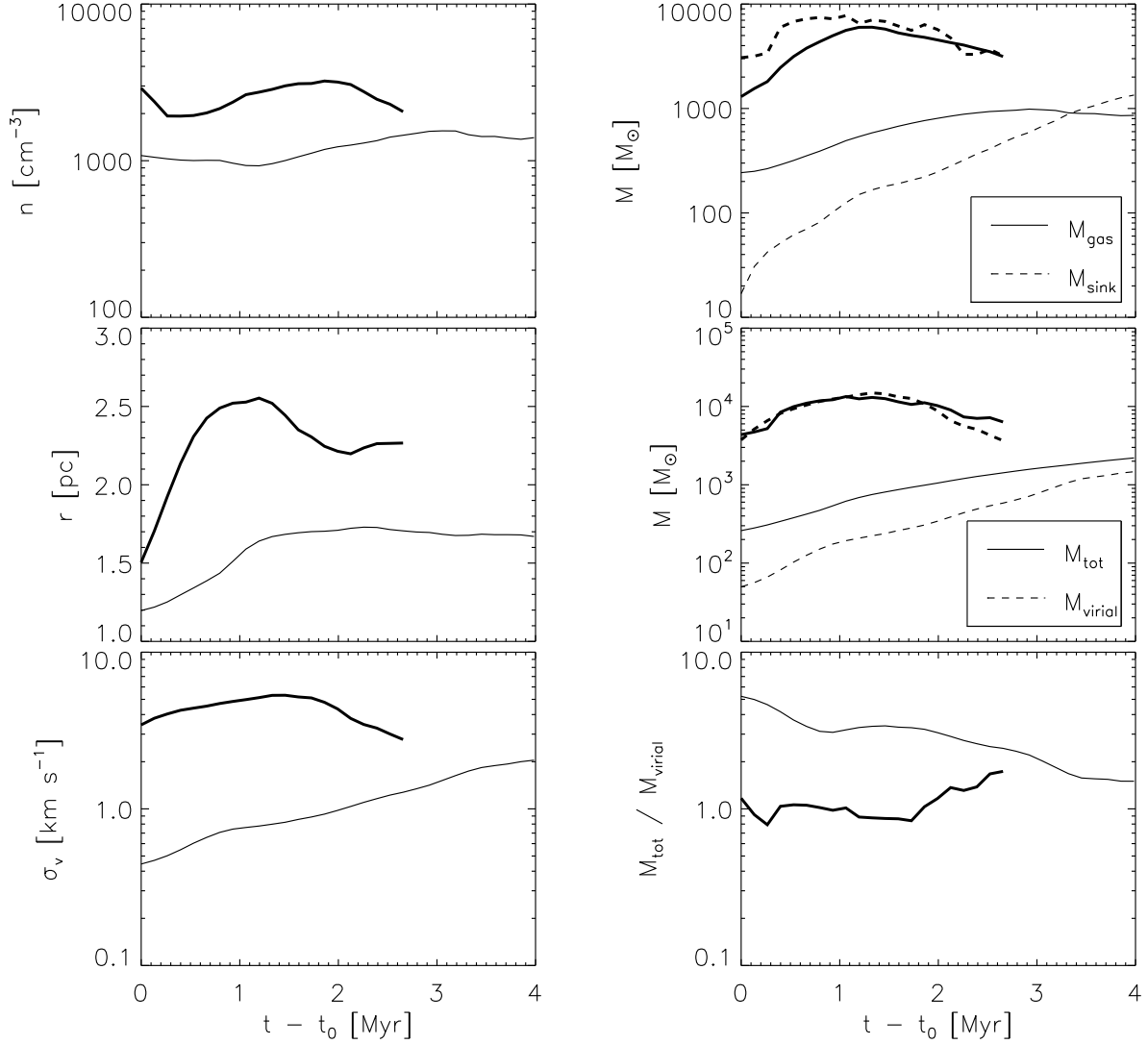


Fig. 3.— Evolution of physical properties of dense gas ($n > n_{\text{th}} = 500 \text{ cm}^{-3}$) in the two star-forming regions analyzed in the simulation. The *thick lines* refer to the “Central Cloud” (CC), and the *thin lines* refer to “Cloud 1” (C1). *Left column*: Evolution of the mean density (*top panel*), size (*middle panel*), and velocity dispersion (*bottom panel*). *Right panel*: Evolution of the dense gas mass and sink mass (*top panel*); evolution of the total (dense gas+sinks) mass and the virial mass (*middle panel*); evolution of the ratio of total to virial mass (*bottom panel*). Note that the starting times t_0 for the evolutionary plots are different for the two regions, being $t_0 = 17.27 \text{ Myr}$ for C1 and $t_0 = 22.58 \text{ Myr}$ for the CC.

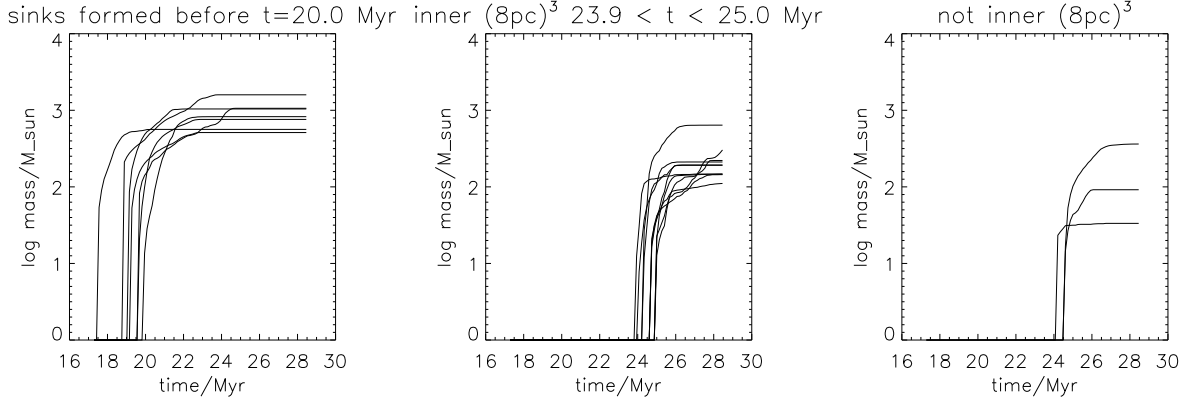


Fig. 4.— Evolution of the most massive sinks formed in the simulation up to $t = 20$ Myr (*left panel*), the most massive sinks formed in the central 8-pc region for $23.9 < t < 25$ Myr (*middle panel*), and those formed outside of the central 8-pc region during the same time interval (*right panel*).

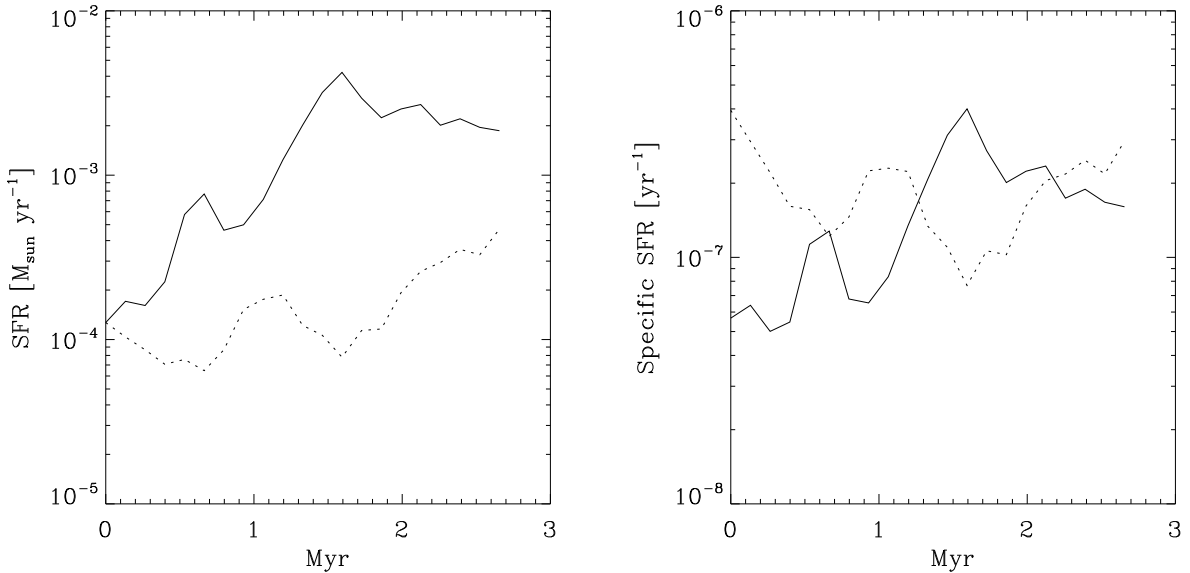


Fig. 5.— Evolution of the SFR and the specific SFR for Cloud 1 (C1, *dotted lines*) and the Central Cloud (CC, *solid lines*).

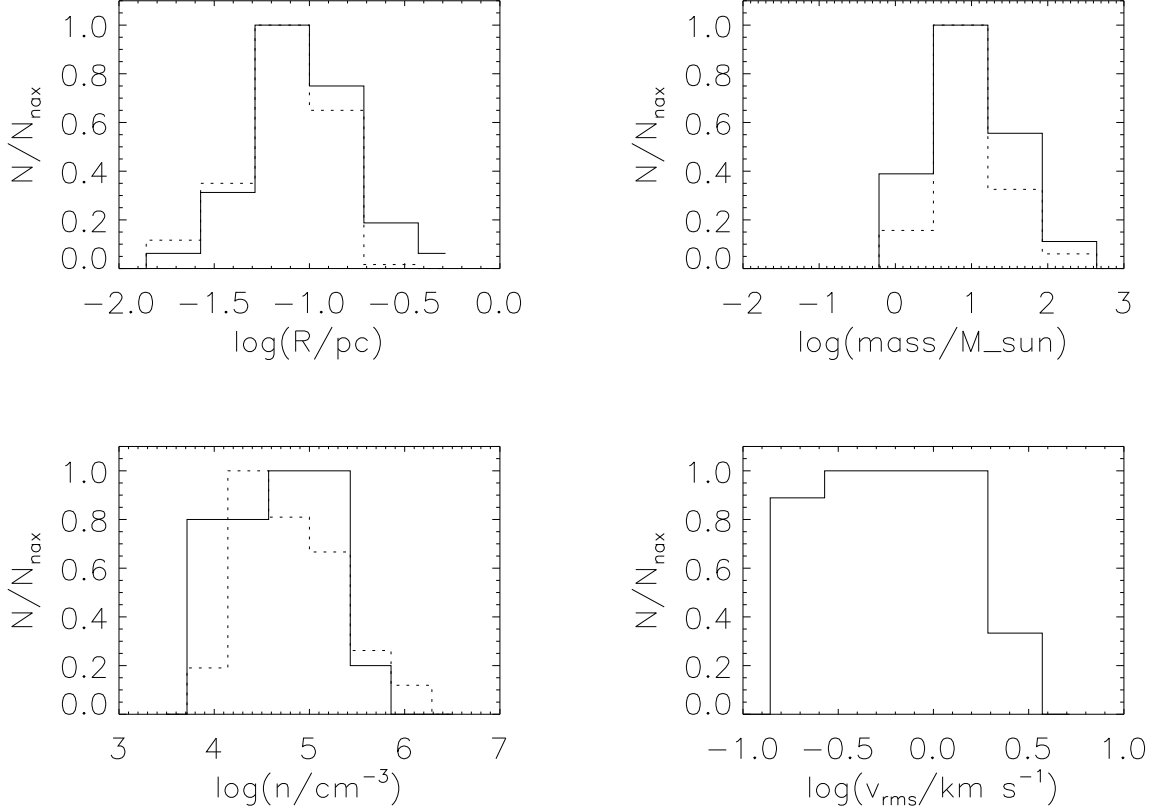


Fig. 6.— Histograms of the size (*top left*), mass (*top right*), mean density (*bottom left*) and three-dimensional velocity dispersion (*bottom right*) of the cores within the Central Cloud of the simulation (*solid lines*) at $t = 23.9$ Myr, at which time the region acquires its most compressed state. The histograms are normalized to their peak values. *Dotted lines*: same for the core sample in Cygnus X reported by Motte et al. (2007), except for the velocity dispersion, since their observations were performed in the 1.2 mm continuum. The distributions are seen to match extremely well for size, mass and mean density.

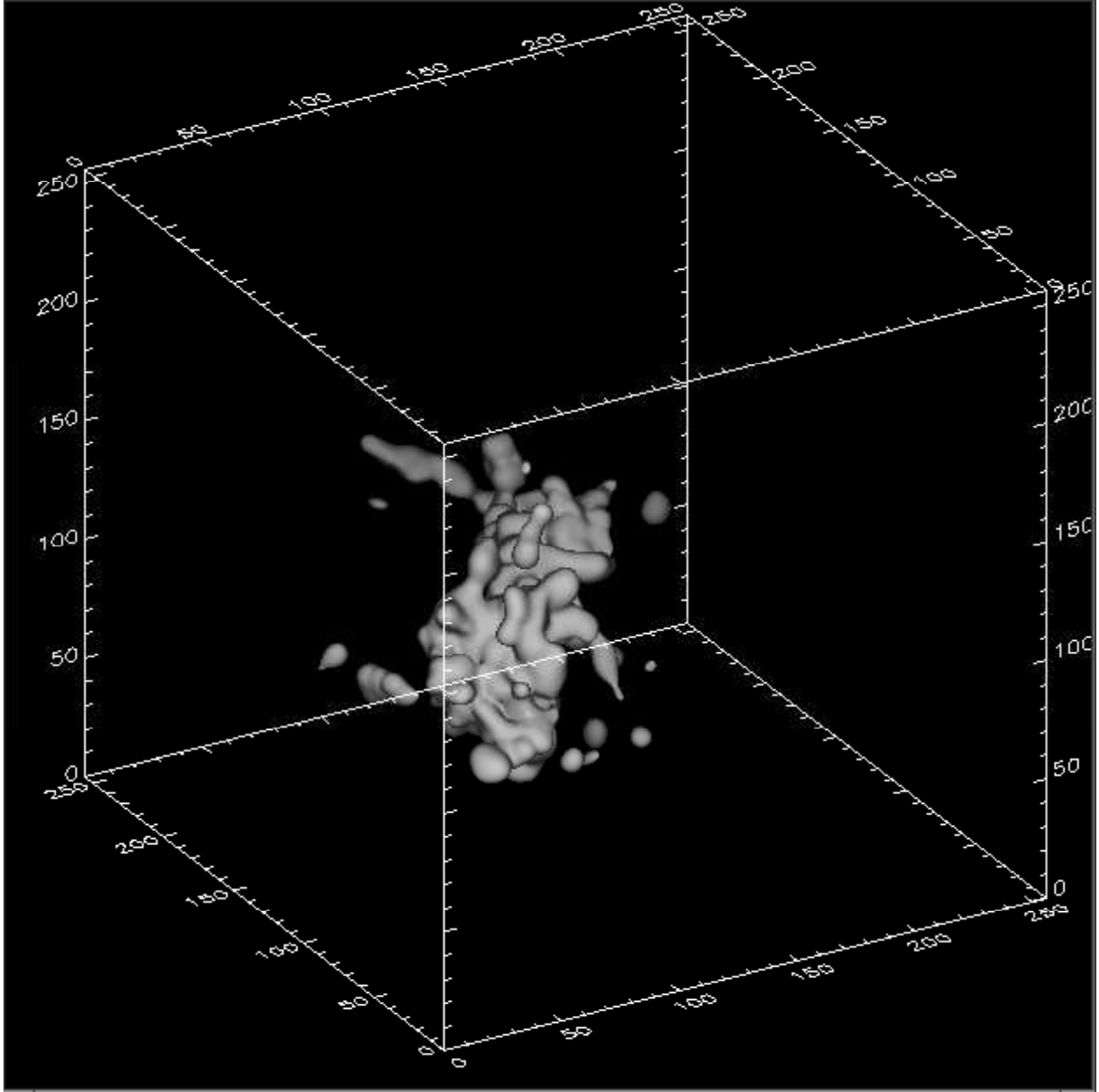


Fig. 7.— Isodensity surface of the structure defined by a density threshold of $n = 7 \times 10^3 \text{ cm}^{-3}$ in the CC.

REFERENCES

- Audit, E. & Hennebelle, P. 2005, *A&A* 433, 1
- Ballesteros-Paredes, J., Hartmann, L. & Vázquez-Semadeni, E. 1999b, *ApJ* 527, 285
- Ballesteros-Paredes, J., Klessen, R. S., & Vázquez-Semadeni, E. 2003, *ApJ*, 592, 188
- Ballesteros-Paredes, J., Vázquez-Semadeni, E., & Scalo, J. 1999a, *ApJ*, 515, 286
- Bally, J., Stark, A. A., Wilson, R. W., & Langer, W. D. 1987, *ApJ*, 312, L45
- Bate, M. R., Bonnell, I. A., & Bromm, V. 2003, *MNRAS* 336, 705
- Beuther, H., Churchwell, E. B., McKee, C. F., Tan, J. C. 2007, in *Protostars and Planets V*, eds. B. Reipurth, D. Jewitt, and K. Keil (Tucson: University of Arizona Press), 165
- Brunt, C. M. 2003, *ApJ*, 583, 280
- Burkert, A., & Hartmann, L. 2004, *ApJ*, 616, 288
- Caselli, P., Benson, P.J., Myers, P.C., & Tafalla, M. 2002, *ApJ*, 572, 238
- Elmegreen, B. 2007, *ApJ*, 668, 1064
- Federrath, C., Klessen, R. S., & Schmidt, W. 2008, *ApJ*, 688, L79
- Field, G., Blackman, E. G, Keto, E. R. 2008, *MNRAS*, 385, 181
- Frisch, U. 1995, *Turbulence. The legacy of A.N. Kolmogorov* (Cambridge: Cambridge University Press)
- Garay, G. & Lizano, S. 1999, *PASP*, 111, 1049
- Goldreich, P., & Kwan, J. 1974, *ApJ* 189, 441

- Hartmann, L., Ballesteros-Paredes, J., & Bergin, E. A. 2001, *ApJ*, 562, 852
- Hartmann, L. & Burkert, A. 2007, *ApJ*, 654, 988
- Hatchell, J., Fuller, G. A., Richer, J. S., Harries, T. J., & Ladd, E. F. 2007, *A&A*, 468, 1009
- Heitsch, F., Burkert, A., Hartmann, L., Slyz, A. D. & Devriendt, J. E. G. 2005, *ApJ* 633,
L113
- Heitsch, F., Hartmann, L., Slyz, A., Devriendt, J., & Burkert, A. 2008, *ApJ*, 674, 316
- Heitsch, F., Slyz, A., Devriendt, J., Hartmann, L., & Burkert, A. 2006, *ApJ*, 648, 1052
- Heitsch, F., Mac Low, M. M., & Klessen, R. S. 2001, *ApJ*, 547, 280
- Hennebelle, P. & Audit, E. 2007, *A&A*, 465, 431
- Hennebelle, P. & Pérault, M. 1999, *A&A* 351, 309
- Hillenbrand, L. A., & Carpenter, J. M. 2000, *ApJ*, 540, 236
- Hoyle, F. 1953, *ApJ*, 118, 513
- Hunter, J. H., Jr., & Fleck, R. C., Jr. 1982, *ApJ*, 256, 505
- Ikeda, N., Sunada, K., & Kitamura, Y. 2007, *ApJ*, 665, 1194
- Jappsen, A.-K., Klessen, R. S., Larson, R. B., Li, Y., and Mac Low, M.-M. 2005, *A&A* 435,
611
- Jijina, J., Myers, P.C., and Adams, F.C. 1999, *ApJS*, 125, 161
- Klessen, R. S. 2001, *ApJ*, 556, 837
- Klessen, R. S., Ballesteros-Paredes, J., Vázquez-Semadeni, E., and Durán-Rojas, C. 2005,
ApJ, 620, 786

- Klessen, R. S., & Burkert, A. 2000, *ApJS*, 128, 287
- Klessen, R. S., & Burkert, A. 2001, *ApJ*, 549, 386
- Klessen, R. S., Heitsch, F., & MacLow, M. M. 2000, *ApJ*, 535, 887
- Koyama, H. & Inutsuka, S.-I. 2002, *ApJ*, 564, L97
- Kurtz, S., Cesaroni, R., Churchwell, E., Hofner, P., Walmsley, C. M. 2000, in *Protostars and Planets IV*, eds. V. Mannings, A. P. Boss, S. S. Russell (Tucson: University of Arizona Press), 299
- Lee, C.W., & Myers, P.C. 1999, *ApJS*, 123, 233
- McKee, C. F., Tan, J. C. 2003, *ApJ*, 585, 850
- Morata, O., Girart, J. M., & Estalella, R. 2005, *A&A*, 435, 113
- Motte, F., Bontemps, S., Schilke, P., Schneider, N., Menten, K. M., Broguire, D. 2007, *A&A*, 476, 1243
- Newman, W.I., & Wasserman, I. 1990, *ApJ*, 354, 411
- Ossenkopf, V., & Mac Low, M.-M. 2002, *A&A*, 390, 307
- Passot, T., Vázquez-Semadeni, E., & Pouquet, A. 1995,
- Peretto, N., Hennebelle, P., André, P. 2007, *A&A*, 464, 983
- Price, D., *PASA*, 24, 159
- Springel, V., Yoshida, N., White, S. D. M. 2001, *New Astron.*, 6, 79
- Stutzki, J., & Güsten, R. 1990, *ApJ*, 356, 513.
- Tachihara, K., Onishi, T., Mizuno, A., & Fukui, Y. 2002, *A&A*, 385, 909

- Tobin, J. J., Hartmann, L., Furesz, G., Mateo, M., & Megeath, S. T. 2009, arXiv:0903.2775
- Vázquez-Semadeni, E., Ballesteros-Paredes, J., & Rodríguez, L.F. 1997, ApJ, 474, 292
- Vázquez-Semadeni, E., González, R. F., Ballesteros-Paredes, J., Gazol, A., & Kim, J. 2008, MNRAS, 390, 769
- Vázquez-Semadeni, E., Gómez, G. C., Jappsen, A. K., Ballesteros-Paredes, J., González, R. F., & Klessen, R. S. 2007, ApJ, 657, 870 (Paper I)
- Vázquez-Semadeni, E., Kim, J., Shadmehri, M. & Ballesteros-Paredes, J. 2005, ApJ, 618, 344
- Vázquez-Semadeni, E., Passot, T., & Pouquet, A. 1995, ApJ, 441, 702
- Vázquez-Semadeni, E., Passot, T., & Pouquet, A. 1996, ApJ, 473, 881
- Vázquez-Semadeni, E., Ryu, D., Passot, T., González, R. F., & Gazol, A., 2006, ApJ, 643, 245
- Walder, R. & Folini, D. 2000 ApSS, 274, 343
- Williams, J.P., de Geus, E.J., & Blitz, L. 1994, ApJ, 428, 693
- Zinnecker, H., & Yorke, H. W. 2007, ARA&A, 45, 481
- Zuckerman, B. & Palmer, P. 1974, ARA&A, 12, 279